Friction Compensation Control for Power Steering

Frédéric Wilhelm, Tsutomu Tamura, Robert Fuchs, *Member, IEEE*, and Philippe Müllhaupt, *Member, IEEE*

***Abstract*— The effects of friction are critical to the dynamics of electric power steering (EPS). On the one hand, friction contributes to the stability of the system and filters some of the disturbances (road vibration, etc.). On the other hand, it negatively affects the driving feel and refrains from accurate positioning of the steering wheel. In addition, for steering manufacturers, friction hinders the development and tuning of the assistance strategy. Therefore, controlling or eventually suppressing friction in EPS is a real challenge. In this paper, a control strategy for the active compensation of friction in a column-assist-type EPS is presented. The assist motor and the electronic control unit are used to cancel the friction effect in order to imitate the behavior of an ideal frictionless system. The feasibility of this strategy is demonstrated on the power column (the upper part of the steering system) using the same information (signals) as that available in an actual product. The proposed control is based on a model of the power column including slip- and load-dependent friction forces. For this purpose, a detailed simulation model, developed and validated in a previous work, is reduced to a lower order model to enable real-time computation. The LuGre model is used to compute both the static and dynamic friction forces with continuous formulation. The control architecture is composed of two cascaded feedback loops. The internal loop estimates the internal friction of the system and compensates for it through the motor input. The external loop contains a frictionless reference model used as a trajectory planner and a linear controller, which attempts to minimize the error between the plant and the reference responses. The stability and the robustness of the control strategy are formally analyzed. Specifically, it is shown that the limit error between the plant and the reference responses can be made arbitrarily small with appropriate values of the gains. Experimental results demonstrate that the control strategy is successful in tracking the frictionless reference trajectory, and confirm the robustness against inaccurate friction parameters.**

***Index Terms*— Automotive components, control nonlinearities, friction, nonlinear control systems, power steering (PS), reduced-order systems, tracking loops.**

I. Introduction

POWER STEERING (PS) is used to provide assistance by augmenting the torque applied on the steering wheel with an external actuator, such that less effort is required from the driver while maneuvering a vehicle. At first, hydraulic PS (HPS) has been the most prevalent system. Due to the hydraulic damping effect, HPS enables a smooth and pleasant steering feel while providing high assistance power. But because of its significant energy consumption [1], it is being increasingly replaced by electric PS (EPS), which is much more energy efficient since power is delivered on demand only [2], [3]. In addition, EPS offers more flexibility for the control due to the higher actuator bandwidth (electric motor) and computational power of modern electric control units. The control of EPS has been studied widely in the literature, in order to ensure the stability of the system at high assist gain [4], [5] and to optimize the steering feel despite the presence of disturbances [6], [7].

Still, the main limitation of EPS is the increase of friction due to the presence of mechanical elements, which negatively affects the driving feel [8]–[10]. In addition, because friction limits the use of linear EPS models, it hinders the development and tuning of the control strategy [5], [7], [11].

To reduce friction, hardware countermeasures are often employed, such as lubrication or mechanical design optimization, but these are often costly and limited. However, because of the fast actuator response, friction can also be actively controlled. Using control to reproduce, despite the presence of friction, an acceptable level of steering feel with reduced tuning workload is thus a real challenge for steering manufacturers. Some solutions already exist to alleviate the friction effects that are usually composed of separate blocks compensating individually each different friction effect (on-center sticking, steering returnability, damping, etc.) [3], [12]. Typically, this superposition of compensation controls leads to a redundancy of functions and a cumbersome tuning phase. Another solution [13] proposes an online estimation and a compensation of the static friction but without taking the dynamic friction into account. Dithering [14] is another method, which uses a high-frequency component added to the control signal in order to prevent the system from sticking. The disadvantage of dithering is that it is intrusive (addition of a signal component) and difficult to tune.

In this paper, a model-based solution is proposed to compensate all friction effects with the consequences of modifying the characteristics of the EPS to that of a linear frictionless system. This active compensation is implemented at the lowest layer of the EPS control. The question of whether obtaining a frictionless steering system is an ultimate goal is left open. In essence, some effects of friction also contribute to reaching an acceptable level of driving feel. The proposed control strategy can be applied to reduce or fully cancel the effects of friction. In the latter case, a higher level of control would

Manuscript received November 13, 2014; revised June 11, 2015; accepted August 22, 2015. Manuscript received in final form September 21, 2015. Recommended by Associate Editor C. Canudas-de-Wit.

F. Wilhelm, T. Tamura, and R. Fuchs are with the Research and Development Center, JTEKT Corporation, Nara 634-8555, Japan (e-mail: frederic_wilhelm@jtekt.co.jp; tsutomu_tamura@jtekt.co.jp; robert.fuchs@jtekt-eu.com).

P. Müllhaupt is with the Laboratoire d'Automatique and the Biorobotics Laboratory, École Polytechnique Fédérale de Lausanne, Lausanne 1015, Switzerland (e-mail: philippe.muellhaupt@epfl.ch).

Color versions of one or more of the figures in this paper are available online at http://ieeexplore.ieee.org.

Digital Object Identifier 10.1109/TCST.2015.2483561

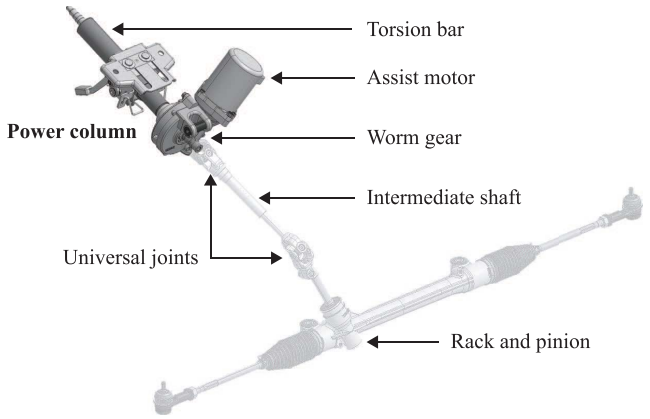

Fig. 1. C-EPS.

be required for the system characteristic to reach a satisfying level of driving feel.

The proposed control strategy is applied to a column-assist type EPS (C-EPS) using the electric motor. For demonstrating the proposed concept, only the power column subsystem is considered (highlighted in Fig. 1), which contains the main assistance components. The strategy is based on a model of the column including a slip- and load-dependent friction torque, built upon reducing a higher order model developed in [9]. The LuGre model is applied for computing the friction forces because of its ability to capture both the static and dynamic effects of friction with a continuous formulation.

This friction compensation control strategy extends the one presented in [10]. Compared with [13], the strategy presented here brings several substantial improvements, including the simplification of the column reduced model from a hybrid formulation (depending on the gear-mesh contact condition) to a single closed-form formulation and the addition of an observer to compute the internal friction forces using the measured outputs. Still, the most important contribution of this paper is the mathematical demonstration of the controller robustness, which leads to a mathematical formula for tuning the controller gains depending on the desired tracking error.

The remaining of this paper is organized as follows. Section II gives a technical explanation of the effects of friction in the EPS dynamic. Section III introduces the simulation model of the power column including friction, which is reduced to a lower order model in Section IV. Both models are validated against the experimental data in Section V. Then, the control strategy is presented along with a stability and robustness analysis in Section VI. The performance and robustness of the control strategy are validated experimentally in Section VII. Finally, the conclusion is given in Section VIII.

II. Friction in EPS

Friction is a nonlinear phenomenon that has been challenging engineers in a wide range of domains. It is characterized by different behaviors in static and dynamic conditions, whether the surfaces in contact are immobile or sliding against each other. The transition between these two conditions is difficult to capture, partly random and not perfectly understood. Due to the difficulty to model the physical causes of friction (surfaces asperities), engineers often rely on empirical models [15].

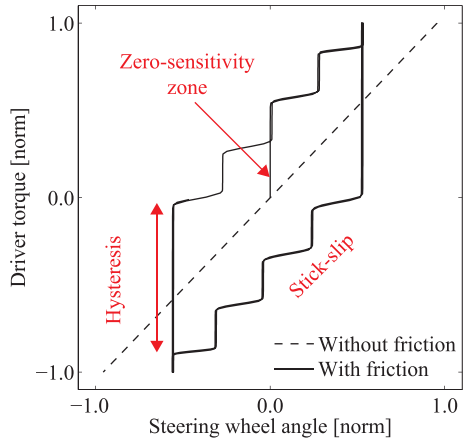

Fig. 2. Friction effects on the EPS static characteristic (simulation).

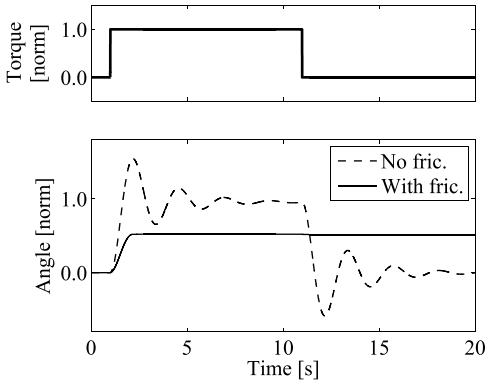

Fig. 3. Friction effects on the EPS dynamic characteristic (simulation).

In EPS, friction is generated at the interface of different mechanical components such as the worm gear, the bearings, the rack and pinion gear, and the joints. When the power column of a C-EPS is considered, friction is predominant at the worm gear due to the preload applied for avoiding backlash. An additional difficulty is that both static and dynamic conditions are solicited due to the regular transitions between rest periods (straight driving) and turning periods.

Typically, the response of a steering system is analyzed using the torque/angle static characteristic (Fig. 2) and the response to a step torque input (Fig. 3). Friction affects the system response in different ways, summarized in the following sections (see [9] for more details).

A. Steering Torque Hysteresis

As shown in Fig. 2, friction contributes to the hysteresis of the system. Although the hysteresis of the torque/angle characteristic is known to be an essential component of steering feel [16], [17], the presence of friction limits the system tunability. Eventually, canceling the entire friction, as proposed by this paper, would endow engineers a greater freedom when tuning the hysteresis characteristic.

B. Zero Sensitivity and Stick Slip

At zero velocity, the driver has to overcome the maximum static friction torque in order to start moving the

steering wheel (vertical line in the middle of Fig. 2). This zero-sensitivity phenomenon refrains from precise control of the vehicle direction, especially during on-center handling [18].

Stick-slip motion, which arises when static friction is higher than dynamic friction (Stribeck effect), also affects the handling negatively. It is illustrated by the stair-shaped portion of the hysteresis loop in Fig. 2 and, in practice, creates an unpleasant jerk steering feel.

C. Steering Returnability

In a steering system, the driver torque is reacted by the tire–road contact force. A self-aligning torque is generated by the suspension geometry (caster angle) and the force distribution on the tire [19]. Seeing from the steering system, this effect is named returnability as the ability of the steering wheel to return to its neutral position when no driver torque is applied. However, in an actual steering system, friction refrains the steering wheel from returning precisely to the neutral position, as illustrated in Fig. 3. Steering returnability is also an important aspect of steering feel [20] and a good indicator for quantifying the effects of friction.

III. Simulation Model of the Power Column

The control strategy developed in this paper is applied to the power column subsystem of a C-EPS, where the main components are as follows.

1) The *torsion bar* to measures the torque $T_{\rm tb}$ between the steering wheel and the worm wheel.
2) The *electric motor* to generates the assistance torque.
3) The *worm gear transmission* (*worm wheel* and *worm gear*) to amplify and transmit the motor torque.
4) The *electronic control unit* to process the sensor signals and control the current of the electric motor.

An extensive literature exists on EPS modeling. However, most of these models are based on the loose assumption that friction can be neglected in order to apply classical linear control theories [21]. The models that contain the friction forces, such as [22], use conditionally based formulation that makes the implementation and the application of control theories difficult. The model proposed here, which has been developed and validated in [9], contains a continuous representation of friction (LuGre model), while also capturing the load dependency due to the gear-meshing contact points. To the best of the authors' knowledge, [23] is the only other publication where the LuGre model is applied to a steering system (steer-by-wire).

A. Power Column System

The power column, including the steering wheel, is a system with three inputs: 1) the motor torque command $T_{\rm mc}$ (control input); 2) the driver torque on the steering wheel $T_{\rm sw}$; and 3) the road load transmitted through the lower shaft $T_{\rm ls}$. Two measurements are available: 1) the angle of the motor shaft $\theta_{\rm ms}$ and 2) the torsion bar torque $T_{\rm tb}$.

The complete model of the power column, or simulation model, is illustrated in Fig. 4. It is composed of four inertias: the steering wheel, the worm wheel, the worm gear, and the motor shaft. The driver input torque and the reaction torque (road load) are directly applied at the steering wheel and the worm wheel, respectively, while the motor command is used to control the motor current and generate the assistance torque. The friction forces at the gear-mesh contact, dominant, are represented with the LuGre model. The other minor friction forces (bearing, etc.) are lumped into this gear-mesh friction and thus are not specifically represented.

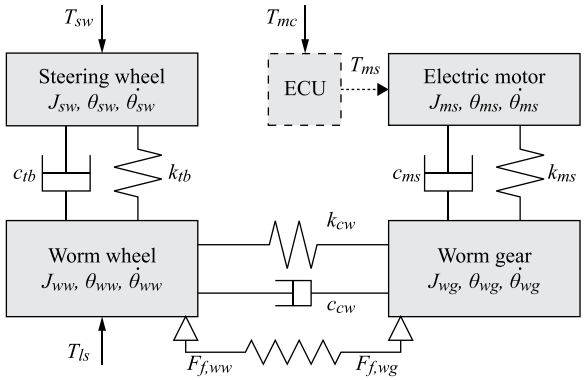

Fig. 4. Simulation model of the power column with steering wheel attached (four inertias).

The equations of the simulation model are detailed as follows.

B. Mechanical Model

The dynamic equations of the four inertias are obtained from Euler's second law of motion as follows:

1) steering wheel
$$J_{\rm sw}\ddot{\theta}_{\rm sw} = T_{\rm sw} - T_{\rm tb} \tag{1}$$
2) worm wheel
$$J_{\rm ww}\ddot{\theta}_{\rm ww} = T_{\rm tb} + T_{c,\rm ww} + T_{\rm ls} \tag{2}$$
3) worm gear
$$J_{\rm wg}\ddot{\theta}_{\rm wg} = T_{\rm mg} + T_{c,\rm wg} \tag{3}$$
4) assist motor rotor
$$J_{\rm ms}\ddot{\theta}_{\rm ms} = T_{\rm ms} - T_{\rm mg} \tag{4}$$

where $J_{\rm xx}$ and $\theta_{\rm xx}$ denote, respectively, the inertia and angle of each component, referred by a specific suffix: sw for the steering wheel, ww for the worm wheel, wg for the worm gear, and ms for the motor shaft. The torques acting on the inertia are the external torques $T_{\rm sw}$ and $T_{\rm ls}$ plus the internal torques:

1) torsion bar torque
$$T_{\rm tb} = k_{\rm tb}(\theta_{\rm sw} - \theta_{\rm ww}) + c_{\rm tb}(\dot{\theta}_{\rm sw} - \dot{\theta}_{\rm ww}) \tag{5}$$
2) coupling between the motor shaft and the worm gear
$$T_{\rm mg} = k_{\rm ms}(\theta_{\rm ms} - \theta_{\rm wg}) + c_{\rm ms}(\dot{\theta}_{\rm ms} - \dot{\theta}_{\rm wg}) \tag{6}$$
3) effective torque $T_{\rm ms}$ generated by the current controller from the motor command $T_{\rm mc}$ (Section III-C);
4) interaction between the worm wheel and the worm gear $T_{c,\rm ww}$ and $T_{c,\rm wg}$ (Section III-D).

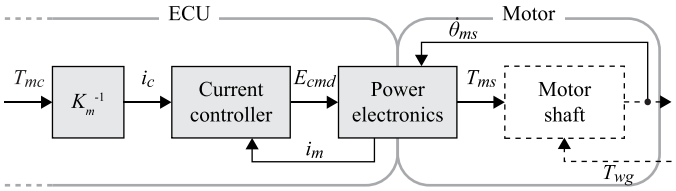

Fig. 5. Model of the motor current loop.

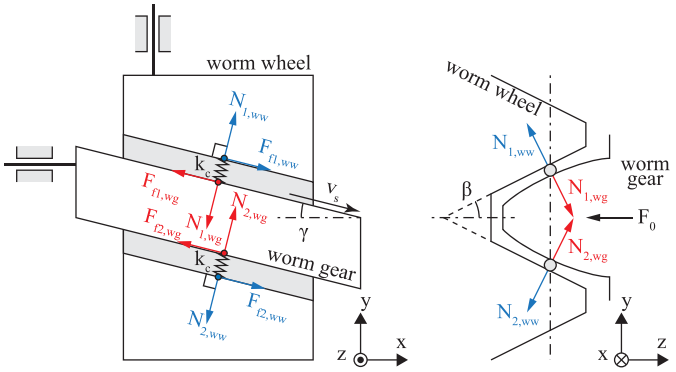

Fig. 6. Worm gear contact at a worm gear tooth meshed between two worm wheel teeth.

C. Current Dynamics of the Motor

The dynamics of the brushless motor (Fig. 5) is represented through an equivalent RL system, including the back electromotive force developed by the rotation of the rotor $\dot{\theta}_{\text{ms}}$

$$E_{\text{cmd}} = R_m i_m + L_m \frac{di_m}{dt} + k_{\text{bemf}} \dot{\theta}_{\text{ms}} \tag{7}$$

where i_m is the current, E_{cmd} is the voltage input, R_m is the motor resistance, L_m is the coil inductance, and k_{bemf} is the back electromotive force constant.

The torque command T_{mc} is first converted into a current command $i_c = T_{\text{mc}}/K_m$, where K_m is the motor constant. Then, the motor current is controlled through the voltage command using a Proporional Integral controller

$$E_{\text{cmd}} = K_p^m (i_c - i_m) + K_i^m \int_0^t (i_c - i_m). \tag{8}$$

The generated torque is equal to $T_{\text{ms}} = K_m i_m$.

D. Gear Mesh Contact Dynamics

The torques $T_{c,\text{ww}}$ and $T_{c,\text{wg}}$ in (2) and (3) generated by the gear meshing are computed using a planar representation at a single tooth [24] illustrated in Fig. 6. In this representation, the plane (x, y) is tangential to the pitch circles and the z-axis is along the common radial direction. The geometry of the contact depends on two angles: the pressure angle β and the lead angle γ. The rotation of the worm wheel corresponds to a translation in the y-direction and the rotation of the worm gear to a translation in the x-direction.

Due to the preload condition, it is assumed that when the system is at rest, the engaged worm gear tooth is in contact with both the upper and lower worm wheel teeth. The system is said to be in the *two-contact- condition*.

The interaction forces between the worm wheel and the worm gear are composed of the normal forces $\vec{N}_{i,\text{xx}}$ and the friction forces $\vec{F}_{\text{fi,xx}}$ (xx $=$ ww, wg) generated at the two contact points (2 cps) $i = 1, 2$ (Fig. 6). The two opposed resultant forces can be expressed as

$$\begin{aligned} \vec{F}_{c,\text{ww}} &= \vec{N}_{1,\text{wg}} + \vec{F}_{f1,\text{wg}} + \vec{N}_{2,\text{wg}} + \vec{F}_{f2,\text{wg}} \\ \vec{F}_{c,\text{wg}} &= \vec{N}_{1,\text{ww}} + \vec{F}_{f1,\text{ww}} + \vec{N}_{2,\text{ww}} + \vec{F}_{f2,\text{ww}}. \end{aligned} \tag{9}$$

The normal forces at the contact points are created by the material deformation represented with springs of constant k_c. The compression of the upper and lower springs can be written $h_1 = (h_0 + dh)^+$ and $h_2 = (h_0 - dh)^+$, respectively, where h_0 is the compression at rest created by the preload and dh is the relative tooth position

$$\begin{aligned} \|\vec{N}_{1,\text{wg}}\| &= \|\vec{N}_{1,\text{ww}}\| = k_c (h_0 + dh)^+ \\ \|\vec{N}_{2,\text{wg}}\| &= \|\vec{N}_{2,\text{ww}}\| = k_c (h_0 - dh)^+. \end{aligned} \tag{10}$$

The positive part $(\ldots)^+ = \max(\ldots, 0)$ accounts for the loss of the contact point, which happens as soon as the compression of the spring becomes null. When one of the 2 cps is lost, the system is said to be in the *one contact point (1 cp) condition*.

The compression at rest h_0 depends on the preload force F_0, the contact stiffness k_c, and the pressure angle β

$$h_0 = \frac{F_0}{2k_c \sin(\beta)}. \tag{11}$$

The relative displacement dh is a function of the relative angular positions of the worm wheel and the worm gear

$$dh = r_{\text{wg}} \theta_{\text{wg}} \sin(\gamma) - r_{\text{ww}} \theta_{\text{ww}} \cos(\gamma) \tag{12}$$

where r_{ww} and r_{wg} are, respectively, the worm wheel and worm gear pitch radii.

Then, the friction force $F_{\text{fi,xx}}$ is the product of the normal force $\|\vec{N}_{i,\text{xx}}\|$ and the friction coefficient μ (because the sliding velocity is the same at each contact point, a single friction coefficient is used)

$$F_{\text{fi,xx}} = \mu \|\vec{N}_{i,\text{xx}}\|. \tag{13}$$

Finally, (9) is rewritten using (10) and (13) and projected on the axes of motion

$$\begin{aligned} F^y_{c,\text{ww}} &= F_C \cos(\gamma) \cos(\beta) - \mu F_N \sin(\gamma) \\ F^x_{c,\text{wg}} &= -F_C \sin(\gamma) \cos(\beta) - \mu F_N \cos(\gamma) \end{aligned} \tag{14}$$

where $F_C(dh)$ is an *equivalent contact force* and $F_N(dh)$ is an *equivalent normal force*

$$F_C(dh) = k_c((h_0 + dh)^+ - (h_0 - dh)^+) \tag{15a}$$

$$F_N(dh) = k_c((h_0 + dh)^+ + (h_0 - dh)^+). \tag{15b}$$

Both functions are represented in Fig. 7, where the contact condition effect is clearly visible. In particular, the normal force is constant in the two-contact-point condition (when one contact force decreases, the other increases by the same amount).

Finally, the forces are converted into torques by multiplication with the pitch radii

$$\begin{aligned} T_{c,\text{ww}} &= r_{\text{ww}} F^y_{c,\text{ww}} \\ T_{c,\text{wg}} &= r_{\text{wg}} F^x_{c,\text{wg}}. \end{aligned} \tag{16}$$

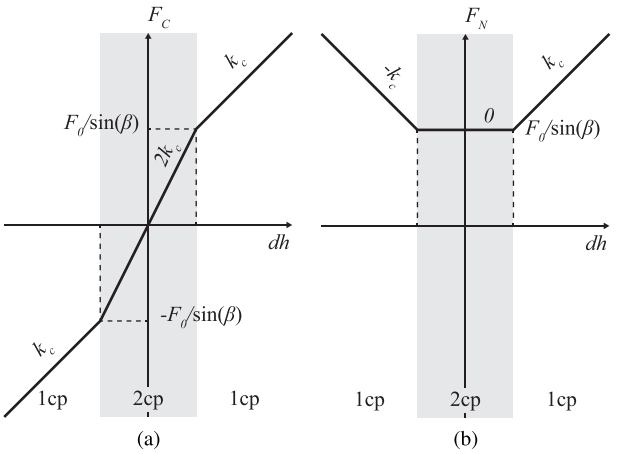

Fig. 7. Equivalent contact and normal force. The system is in the 2 cp condition when $|dh| \leq h_0$ and in the 1 cp condition when $|dh| > h_0$. (a) Equivalent contact force F_C. (b) Equivalent normal force F_N.

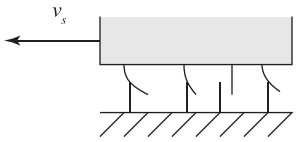

Fig. 8. Contact bristles. The friction force is created by the bristle deflection.

E. Friction Model

A model is used for computing the friction coefficient μ at the gear mesh. Various representations can be found in [15], including classical conditional and dynamic formulations. The main challenge in representing the friction is related to the difference between static (stiction) and dynamic conditions (speed-dependent friction). Because EPS often transit between static and dynamic regimes (on-center control versus cornering), a friction model able to represent and alternate between each condition is required.

The LuGre model, resulting from a collaboration between the Lund Institute of Technology and the University of Grenoble [25], answers this requirement. It is based on a representation of the contact points as elastic bristles (Fig. 8) and requires the introduction of a new state variable. A major interest of the LuGre model is to depend solely on the sliding velocity while being able to represent the main friction phenomena (stiction, coulomb friction, etc.) with a continuous formulation. Because it avoids a hybrid conditional formulation, it is easy to implement for simulation and control applications, while enabling standard stability theories [26].

In most applications of the LuGre model, the normal load at the contact is constant and the friction force F_f is directly computed in the equations. Here, however, the load changes with the contact condition [Fig. 7(b)]. Therefore, as suggested in [26] and applied in [27], the LuGre model is used to compute a friction coefficient μ, multiplied by the load-dependent normal force F_N in (14).

With this representation, the friction forces are created by the average deflection of the bristles, represented by a state variable z. The formulation of the LuGre model is

$$\dot{z} = v_s - \sigma_0 \frac{|v_s|}{g(v_s)} z \tag{17a}$$

$$\mu = \sigma_0 z + \sigma_1 \dot{z} + f(v_s) \tag{17b}$$

where the sliding velocity v_s between the two surfaces (worm gear and worm wheel) as input, the friction coefficient μ as output, σ_0 is the bristle stiffness, σ_1 is the bristle damping, and $f(v_s)$ is the viscous friction coefficient. The denominator $g(v_s)$ represents the steady-state absolute value of the dry friction. The dependence on the velocity v_s allows accommodating a higher coefficient of static friction than that of the dynamic friction (Stribeck effect). A typical form [15] is

$$g(v_s) = \mu_c + (\mu_{\text{ba}} - \mu_c) e^{-\left(\frac{v_s}{v_{\text{stb}}}\right)^2} \tag{18}$$

where μ_{ba} is the static or *break-away* friction coefficient and μ_c is the dynamic *coulomb* friction coefficient with a transition around the Stribeck velocity v_{stb}.

Using (17) and (18), it can be ensured that the state z remains bounded with

$$\sigma_0 z \in [-\mu_{\text{ba}}, \mu_{\text{ba}}].$$

Indeed, it can be observed from (17a) that $\sigma_0 z = \mu_{\text{ba}}$ implies $\dot{z} < 0$ and $\sigma_0 z = -\mu_{\text{ba}}$ implies $\dot{z} > 0$.[1]

However, the derivative $\dot{z}$ and therefore the second term of (17b) can grow unbounded with the sliding velocity v_s. In general, the LuGre model is known to have implementation issues at high sliding velocity and several modifications have already been proposed to address them (see [28]). Here, the following modification of (17b) is proposed:

$$\mu = \text{sat}_{g(v_s)} (\sigma_0 z + \sigma_1 \dot{z}) + f(v_s) \tag{19}$$

using the saturation function defined by

$$\text{sat}_\delta(x) = \begin{cases} -\delta, & \text{for } x < -\delta \\ x, & \text{for } |x| \leq \delta \\ \delta, & \text{for } x > \delta. \end{cases} \tag{20}$$

With this modification, the dry friction represented by the first two terms $\sigma_0 z + \sigma_1 \dot{z}$ is ensured to remain bounded (in absolute value) by its steady-state value $g(v_s)$.

Finally, the LuGre model is used to compute the friction coefficient at the gear-mesh contact. The sliding velocity v_s is given by

$$v_s = r_{\text{ww}} \dot{\theta}_{\text{ww}} \sin(\gamma) + r_{\text{wg}} \dot{\theta}_{\text{wg}} \cos(\gamma). \tag{21}$$

Friction parameters of the current power column have been identified experimentally or tuned manually (Appendix A).

The gear-mesh contact model presented in Section III-D along with the LuGre friction model enables the computation of the torques generated at the gear-mesh contact (16).

IV. Reduced Model

In order to facilitate the controller design and to enable real-time computation, the order of the model is reduced by

[1] At the condition that z is initialized within that interval. If z is initialized outside the interval (which has no physical meaning), it can be shown with (17a) that z will converge asymptotically to the interval at the condition that $\int_o^\infty |v(t)|/g(v(t))dt = \infty$.

neglecting overly stiff elements and removing high cutoff frequencies. The reduced model, or *control model*, is made of one inertia with slip- and load-dependent friction.

A. Neglecting the Current Dynamics

The current dynamics of the motor is significantly faster than the working bandwidth (30 Hz) of the column. Therefore, it is neglected and the motor generated torque $T_{\rm ms}$ is supposed to be equal to the command $T_{\rm mc}$.

B. Lumping the Assist Motor Shaft and the Worm Gear

The compliance of the motor shaft (represented by the stiffness $k_{\rm ms}$ and damping $c_{\rm ms}$) is small compared with that of the other mechanical links and generates a dynamics that is above the working bandwidth. Therefore, the two inertia can be lumped together in order to remove 1 DOF

$$\theta_{\rm ms}(t) \equiv \theta_{\rm wg}(t). \tag{22}$$

C. Neglecting the Contact Dynamics

Similarly, the dynamics generated by the stiffness k_c of the material deformation at the gear mesh is assumed to be higher than the working bandwidth. Therefore, the contact dynamics are neglected and it is assumed that the worm wheel position is equal to the worm gear position scaled by the gear ratio i

$$\theta_{\rm ww}(t) \equiv i\,\theta_{\rm wg}(t) \tag{23}$$

where i depends on the two pitch radii and the lead angle

$$i = \frac{r_{\rm ww}}{r_{\rm wg}}\cot(\gamma). \tag{24}$$

Namely, the power column is reduced to a single inertia $J = J_{\rm ww} + i^2(J_{\rm wg} + J_{\rm ms})$, whose angle is noted θ.

Although the worm wheel and worm gear have been lumped together, the effect of the contact condition should be computed, since it affects the mesh friction forces through the equivalent normal force (15b). Since neglecting the dynamics of the gear-mesh contact is equivalent to assuming that these dynamics are always in steady state, the equilibrium value of dh, depending on the external torques, is used. This leads to an expression of the form

$$dh = f(T_{\rm tb}, T_{\rm mc}, T_{\rm ls}) \tag{25}$$

which is developed in Appendix B.

D. Removing the Steering Wheel

The reduced model of the power column directly uses the torsion bar torque $T_{\rm tb}$ as input. Therefore, the steering wheel is not included.

E. Addition of a Vehicle Model

Unlike the torsion bar input, the reverse input at the lower shaft is not measured. However, based on the knowledge of the suspension geometry and the tire property, it is possible to estimate this torque with a vehicle model. As a first approach, a simple spring-damper shaft has been used to represent the self-aligning reaction of the wheel

$$T_{\rm ls} = -k\theta - c\dot\theta \tag{26}$$

where k is the stiffness and c is the damping of the vehicle model. In future development steps, a more accurate model may be used [29], [30].

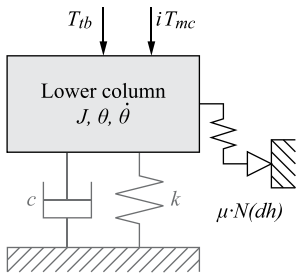

Fig. 9. Power column reduced model with vehicle model applied at the bottom shaft (in grayscale).

F. Sliding Velocity at the Gear Mesh

Using (21), (23), and (24), the sliding velocity at the gear mesh for the reduced model is obtained

$$v_s = \frac{r_{\rm ww}\dot\theta}{\sin(\gamma)}. \tag{27}$$

Since the sliding velocity is proportional to the velocity $\dot\theta$ of the main shaft, a change of variable enables using $\dot\theta$ instead of v_s in the LuGre model (17).

G. Equations of the Reduced Model

Under the assumptions made in the previous sections, the equations of the reduced model are

$$\begin{aligned} J\ddot\theta &= T_{\rm tb} + i\,T_{\rm mc} - k\theta - c\dot\theta - \mu N(dh) \\ \dot z &= \dot\theta - \sigma_0\frac{|\dot\theta|}{g(\dot\theta)}z \end{aligned} \tag{28}$$

where μ is the friction coefficient computed with (19) and

$$N(dh) = \frac{r_{\rm ww}}{\sin(\gamma)}F_N(dh) \tag{29}$$

is an *equivalent normal torque* that depends on the gear load condition dh. The use of the piecewise linear function $N(dh)$ and the calculation of the contact condition with (25) avoids the hybrid formulation developed in [10] for the same system. In particular, the dependency of dh with the input torques enables avoiding the introduction of an efficiency coefficient.

The reduced model, represented in Fig. 9, is therefore described by three state variables θ, $\dot\theta$ (column angular position and velocity), and z (friction state).

V. Model Validation

In this section, the open-loop performance of the plant power column is analyzed and compared with the computed responses of both the simulation and the reduced models as well as experimental measurement obtained from a dedicated test bench. Report on the validation of the complete simulation model presented in Section III was given in [9].

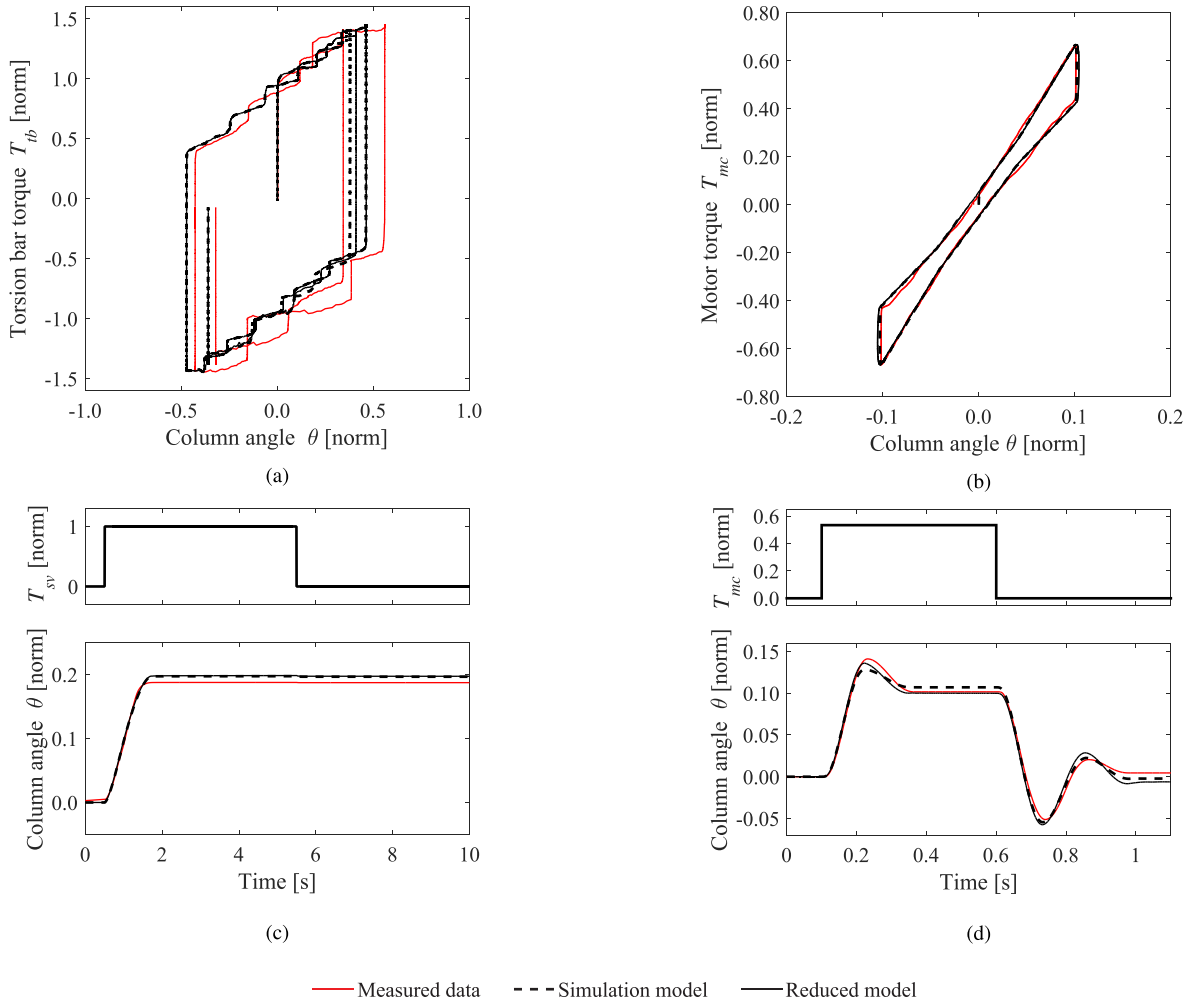

Fig. 10. Plant response with and without friction compensation compared with the reference model response. (a) Static validation for driver input (0.01-Hz sine wave). (b) Static validation for motor input (0.01-Hz sine wave). (c) Dynamic validation for driver input (steer and release). (d) Dynamic validation for motor input (steer and release).

A. Description of the Test Bench

The test bench (Fig. 11) is composed of a mass-produced C-EPS power column, a servomotor to generate the driver input using a torque command signal T_{sv} and a linear spring to simulate the road load. When using the driver torque input, a spring of small stiffness coefficient is chosen to highlight the transition between static and dynamic frictions. When using the motor input (which can generate higher torque at the column due to the reduction gear), a spring of higher stiffness and torque range is used to highlight the loss of 1 cp at the mesh.

B. Static Validation

The quasi-static responses of the power column are plotted in Fig. 10(a) (driver input) and (b) (motor command input). Due to friction, both responses depict a hysteresis, in which height corresponds to the zero-sensitivity zone.

In Fig. 10(a), due to the low load stiffness used, the transition between static and dynamic frictions is clearly visible (stick-slip motion) and well reproduced by both the simulation and the reduced models. However, due to the random nature of friction, the exact positions of these transitions hardly correlate between the simulation and the plant.

In Fig. 10(b), the transition between the 2 cp conditions and the 1 cp condition is visible through the increase of the hysteresis height at high motor torque. In the 2 cp conditions, the equivalent normal force applied at the gear meshing [Fig. 7(b)] is constant, therefore the hysteresis height remains constant (parallel lines). When the torque increases, 1 cp is lost and the normal force rises with the gear load, resulting in higher friction and greater hysteresis.

In both Fig. 10(a) and (b), it can be seen that the simulation and the reduced models have almost identical responses. In particular, the loss of contact point is accurately reproduced by the models in Fig. 10(b), which validates the load torque dependency.

C. Dynamic Validation

The dynamic responses are shown in Fig. 10(c) (driver input) and (d) (motor command input), generated by applying a pulse signal at the servo motor torque command T_{sv} and assist motor torque command T_{mc}, respectively.

In Fig. 10(c), the damping effect of friction and the poor steering returnability are well reproduced by both the complete and the reduced models. After the step input, the system takes

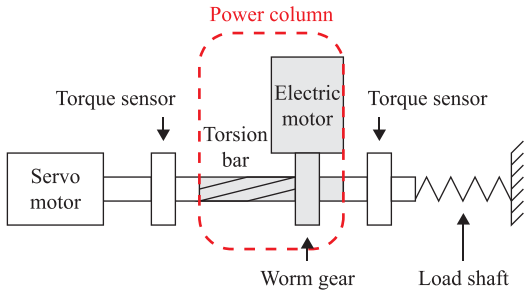

Fig. 11. Power column test bench.

around 1 s to stabilize and remains blocked in its final state even when the input torque is released.

In Fig. 10(d), due to the high load, the effect of static friction on the steering returnability is relatively less visible. The system depicts a second-order like response with a higher damping for torque step up due to the transition to the 1 cp condition. The load-dependent friction model enables both the complete and the reduced models to capture this behavior.

Again, in both cases, the simulation and the reduced models have almost identical responses.

These experiments validate both the simulation and the reduced models to the lower order model.

VI. Control Strategy

The proposed control strategy explores the possibility of canceling the effects of friction by adding an equivalent but opposite torque to the assist motor command, which value is estimated using the reduced model presented above.

A. Control Objectives

Given the different torque inputs (driver torque, assist torque, and road reaction torque), the objective of the proposed strategy is to remove the effects of the friction forces in the column, which are dominant at the worm gear meshing. In other words, the closed-loop response of the power column should have an input/output characteristics similar to that of the same column, but also be frictionless.

B. Control Design

The proposed control strategy is presented in Fig. 12. It is composed of two cascaded loops.

1) Internal Loop: The internal loop (dashed frame) contains a state observer of the power column. It is derived from the reduced model (Section IV) where a linear correction term is added, using the measure of the assist motor angle sensor (position θ_{am} and velocity $\dot{\theta}_{\text{am}}$)

$$\begin{aligned} J\ddot{\tilde{\theta}} &= T_{\text{tb}} + i\,T_{\text{mc}} - k\tilde{\theta} - c\dot{\tilde{\theta}} - \tilde{\mu}N(d\tilde{h}) \\ &\quad + l_p(i^{-1}\theta_{\text{am}} - \tilde{\theta}) + l_v(i^{-1}\dot{\theta}_{\text{am}} - \dot{\tilde{\theta}}) \\ \dot{\tilde{z}} &= \dot{\tilde{\theta}} - \sigma_0 \frac{|\dot{\tilde{\theta}}|}{g(\dot{\tilde{\theta}})}\tilde{z} \end{aligned} \tag{30}$$

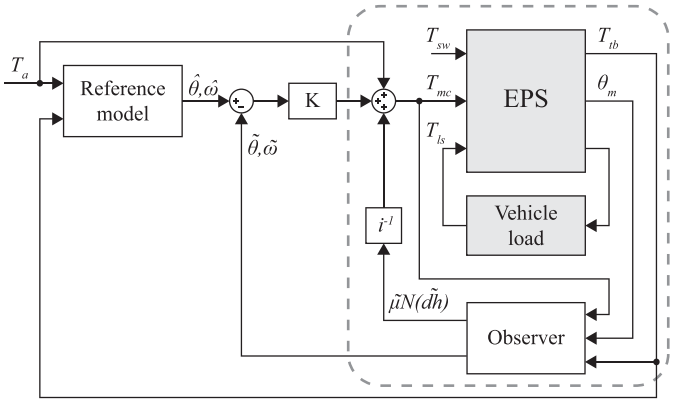

Fig. 12. Friction compensation control strategy.

with

$$\tilde{\mu} = \text{sat}_{g(\dot{\tilde{\theta}})}(\sigma_0\tilde{z} + \sigma_1\dot{\tilde{z}}) + f(\dot{\tilde{\theta}}). \tag{31}$$

Using this estimation, a torque equal but opposed to the friction torque $\tilde{\mu}N(d\tilde{h})$ is added to the assist motor command.

2) External Loop: The external loop contains a model following the control to ensure that the plant tracks an angular reference trajectory $\hat{\theta}(t)$ generated by a reference model of the power column. The reference model is identical to the reduced model in Section IV but without the friction forces and computes the desired angular trajectory $\hat{\theta}(t)$

$$J\ddot{\hat{\theta}} = T_{\text{tb}} + i\,T_a - k\hat{\theta} - c\dot{\hat{\theta}}. \tag{32}$$

Using the difference between the reference column states $\hat{\theta}$ and $\dot{\hat{\theta}}$ and the observed column states $\tilde{\theta}$ and $\dot{\tilde{\theta}}$, a linear correction torque is added to the motor torque command.

Finally, the control command given to the electric motor is composed of the desired assistance torque T_a plus the correction torques from the internal and external loops

$$T_{\text{mc}} = T_a + i^{-1}(\tilde{\mu}N(d\tilde{h}) + k_p(\hat{\theta} - \tilde{\theta}) + k_v(\dot{\hat{\theta}} - \dot{\tilde{\theta}})) \tag{33}$$

where k_p and k_v are the gains of the correction torque. The division by the gear ratio i is necessary to anticipate the motor torque amplification by the gear ratio.

This configuration corresponds to the angular control of the power column, also called admittance control [31]. Torque control [32], also called impedance control, is another possible approach for steering systems, appropriate for steer-by-wire in particular [33].

C. Stability and Robustness Analysis

It is known that the interaction between actual friction and friction compensation produces limit cycles caused by velocity estimation errors [34] or by friction parameter's inaccuracy [35]. Similar to [34], it is shown here that the tracking error reaches a limit set whose size increases with the friction misestimation but decreases with the gains of the controller. Therefore, if a bound on the friction misestimation is known, the gains can be chosen to obtain an appropriate level of robustness. The robustness against inaccuracy of other

parameters (inertia, stiffness, damping, etc.) is not considered here.

Because the effects of friction are particularly critical in on-center driving condition, where the steering velocity and the worm gear load remain small, the demonstration is made under two assumptions.

1) The system remains in the 2 cp conditions, therefore the gear load $N(dh)$ remains constant and is noted N.
2) The angular velocity remains small enough such that the nonlinear viscous friction $f(\dot{\theta})$ (Appendix A) is linearly approximated and noted $\sigma_2\dot{\theta}$.

Consider the closed-loop system (plant and controller) in which the plant is represented with the reduced model (28)

$$\begin{aligned} J\ddot{\theta} &= T - k\theta - c\dot{\theta} + k_p(\hat{\theta}-\tilde{\theta}) + k_v(\dot{\hat{\theta}}-\dot{\tilde{\theta}}) \\ &\quad + \tilde{\mu}N - \mu N \\ J\ddot{\tilde{\theta}} &= T - k\tilde{\theta} - c\dot{\tilde{\theta}} + k_p(\hat{\theta}-\tilde{\theta}) + k_v(\dot{\hat{\theta}}-\dot{\tilde{\theta}}) \\ &\quad + l_p(\theta-\tilde{\theta}) + l_v(\dot{\theta}-\dot{\tilde{\theta}}) \\ J\ddot{\hat{\theta}} &= T - k\hat{\theta} - c\dot{\hat{\theta}} \end{aligned} \tag{34}$$

where $T = T_{\text{tb}} + iT_a$ represents the total input torque.

Considering the error variables $\varphi = \theta - \tilde{\theta}$ and $\tilde{\varphi} = \tilde{\theta} - \hat{\theta}$, system (34) rewrites

$$\begin{aligned} J\ddot{\varphi} &= -(k+l_p)\varphi - (c+\sigma_2 N + l_v)\dot{\varphi} + u \\ J\ddot{\tilde{\varphi}} &= -(k+k_p)\tilde{\varphi} - (c+k_v)\dot{\tilde{\varphi}} + l_p\varphi + l_v\dot{\varphi} \end{aligned} \tag{35}$$

where

$$u = \left(\text{sat}_{\tilde{g}(\dot{\tilde{\theta}})}(\sigma_0\tilde{z} + \sigma_1\dot{\tilde{z}}) - \text{sat}_{g(\dot{\theta})}(\sigma_0 z + \sigma_1\dot{z})\right)N \tag{36}$$

is the compensation error of the dry friction (the viscous friction $\sigma_2 N$ is lumped into the system damping). In particular, u is bounded with

$$\|u\|_{\mathcal{L}_\infty} = \sup_{t\geq 0}|u(t)| \leq (\mu_{\text{ba}} + \tilde{\mu}_{\text{ba}})N \tag{37}$$

where μ_{ba} and $\tilde{\mu}_{\text{ba}}$ are, respectively, the actual and estimated static friction coefficients (which can be different due to identification errors or variation of μ_{ba} caused by wear or environmental conditions).

System (35) is then regarded as a linear system with input u and output $\theta - \hat{\theta} = \varphi + \tilde{\varphi}$ (tracking error between the plant and the reference models). From the theory of linear systems, it is known that (35) can be written as a convolution product

$$\varphi + \tilde{\varphi} = h * u + o(1) = \int_0^t h(t-\tau)u(\tau)d\tau + o(1) \tag{38}$$

where h is the impulse response and $o(1)$ the solution with $u = 0$ and given initial conditions (homogeneous equation). Because (35) is Hurwitz, this terms decreases exponentially to zero.

Then, knowing the bound on the input u, a bound on the output $\varphi + \tilde{\varphi}$ can be obtained. Indeed, it can be shown [36, p. 199] that

$$|h * u| \leq \|h\|_{\mathcal{L}_1}\|u\|_{\mathcal{L}_\infty} \tag{39}$$

where

$$\|h\|_{\mathcal{L}_1} = \int_0^\infty |h|$$

is the $\mathcal{L}_1$ norm of h, which is properly defined since (35) is Hurwitz.

The value of $\|h\|_{\mathcal{L}_1}$ is fastidious to compute. However, the case where the two second-order systems in (35) are critically damped is treated in Appendix C. In this case, the gains l_p, l_v, k_p, and k_v are chosen by pole placement

$$\begin{aligned} C_1 &= \frac{c+\sigma_2 N + l_v}{2J} = \sqrt{\frac{k+l_p}{J}} \\ C_2 &= \frac{c+k_v}{2J} = \sqrt{\frac{k+k_p}{J}} \end{aligned} \tag{40}$$

such that $-C_1$ and $-C_2$ are the two (repeated) poles of (35), located on the negative real axis. Increasing C_1 improves the observer correction while increasing C_2 improves the reference model tracking.

In this condition, it results (Appendix C) that

$$\|h\|_{\mathcal{L}_1} \leq \left(\frac{1}{JC_1^2} + \frac{1+4e^{-1}}{JC_2^2}\right).$$

Finally, the tracking error of the reference model verifies

$$|\theta(t) - \hat{\theta}(t)| \leq \left(\frac{1}{k+l_p} + \frac{1+4e^{-1}}{k+k_p}\right)\|u\|_{\mathcal{L}_\infty} + o(1). \tag{41}$$

From this result, it can be seen that the tracking error eventually increases with the friction misestimation $\|u\|_{\mathcal{L}_\infty}$ and decreases with the correction gains k_p, k_v, l_p, and l_v. Therefore, the higher the gains, the higher the robustness against inaccurate friction parameters. In practice, the size of the gains will be limited by practical issues, such as sensor noise, actuator bandwidth, and sampling time. Taking into account these limits to obtain the appropriate gain tuning is an interesting extension left open for future work.

VII. Results

The presented control strategy has been implemented and tested on the test bench equipped with the C-EPS power column. The same experiments (static and dynamic) as those of Section V have been made. Then, the robustness is addressed by introducing friction parameter's errors and varying the values of the gains. Finally, the roles and contributions of the two control loops are discussed and illustrated.

A. Gain Tuning

The gains l_p, l_v, k_p, and k_v are chosen by placing the poles C_1 and C_2 according to (40) depending on the desired tracking performance (41) and the hardware limitations.

Since C_1 corresponds to the observer correction, it is mainly limited by the sampling time and the noise of the motor angle sensor (resolver). Because the motor resolver of the considered C-EPS has almost no noise, the value $C_1 = 110$ Hz is selected.

The pole C_2 determines how well the plant tracks the reference model and is mainly limited by the motor response. The value $C_2 = 30$ Hz is used since it is within the motor bandwidth and should ensure a tracking error (41) below 2°.

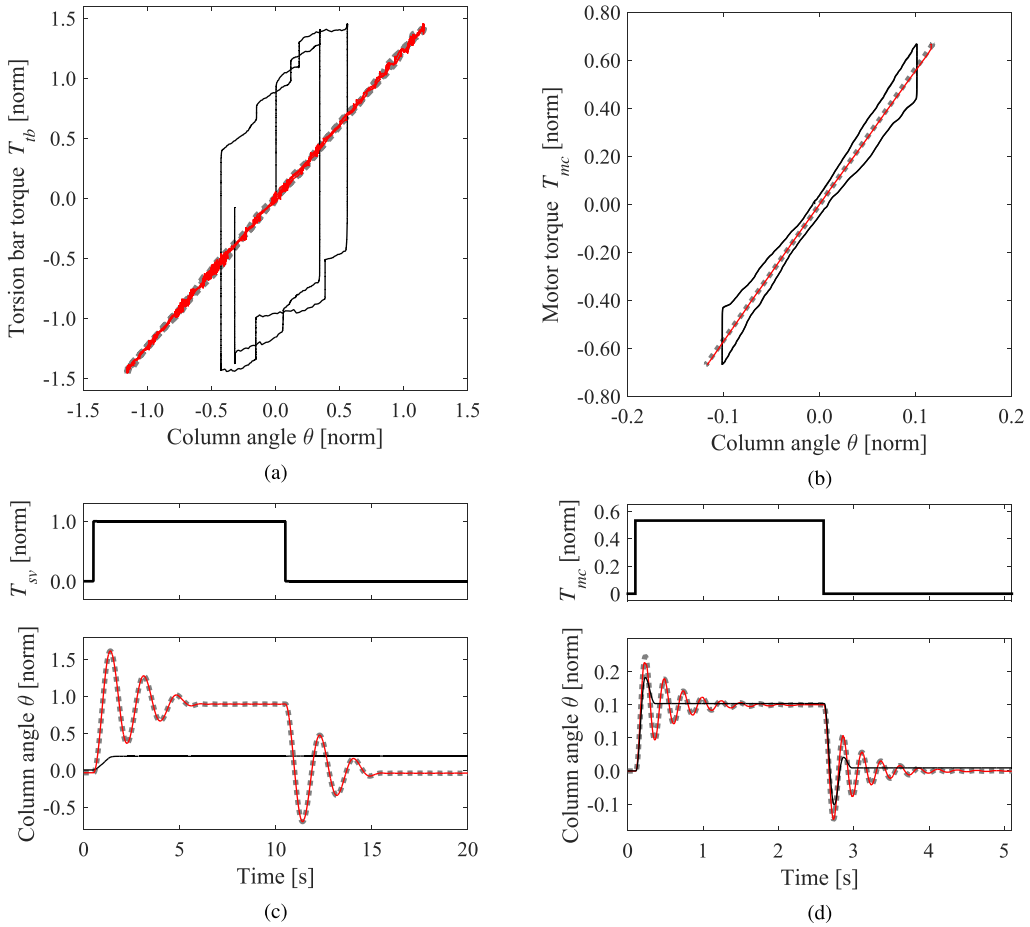

Fig. 13. Plant response with and without friction compensation compared with the reference model response. (a) Static response for driver input (0.01-Hz sine wave). (b) Static response for motor input (0.01-Hz sine wave). (c) Dynamic response for driver input (steer and release). (d) Dynamic response for motor input (steer and release).

B. Static Response

Again, the quasi-static angle–torque characteristic of the power column has been generated using a sinusoidal torque input of low frequency (0.01 Hz) applied on the driver torque input [Fig. 13(a)] and the assist motor input [Fig. 13(b)]. Low and high load stiffnesses are, respectively, applied.

It can be seen that with the proposed control, the plant response accurately tracks the reference response and depicts a linear and frictionless characteristic. In particular, the hysteresis is significantly reduced and the sensitivity is increased. Fig. 13(b) shows that the control performance is not affected by the variation of the load when 1 cp is lost.

C. Dynamic Response

The dynamic responses of the power column, generated from rectangular input signals corresponding to steer and release periods, are shown in Fig. 13(c) for the driver input and Fig. 13(d) for the motor input.

The power column with the control strategy accurately follows the linear underdamped second-order response of the reference model. In particular, the damping is reduced, the sensitivity is increased (a higher value is reached during the steering phase) and the steering returns to the neutral position when the input torque is released. Due to the high gains, the limit cycles in steady-state condition [34] are not visible.

D. Robustness

Since the control strategy is model based, it requires an accurate knowledge of the parameters, in particular those related to friction. While other design parameters (inertia, gear ratio, etc.) are accurately defined, friction parameters are difficult to estimate because friction is irregular and changes over time due to wear and environmental conditions. It is important to ensure that the control strategy remains robust toward these variations. In addition, friction differs between different products due to manufacturing dispersion, thus a sufficient level of robustness is necessary for avoiding the calibration of each column individually.

The bound on the tracking error (41) enables estimating qualitatively the effects of inaccurate friction parameters. In this case, the perturbation term (36) increases along with the limit tracking error. However, (41) can be reduced by increasing the values of the control gains k_p, k_v, l_p, and l_v.

A sensitivity analysis demonstrated that the static parameters μ_{ba} and μ_c of the LuGre model are dominant. Therefore, the system robustness has been validated by varying these parameters in the reduced model relatively to the plant identified parameters by factors of 0 (no friction model), 1 (matching friction model), and 2 (twice the real friction). The first and third cases correspond, respectively, to the worst cases of friction undercompensation and the friction overcompensation,

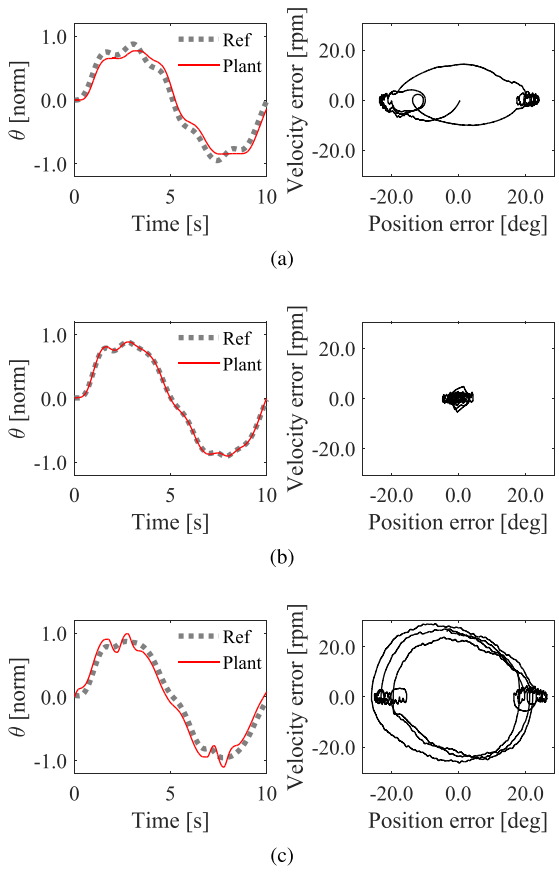

Fig. 14. Angular tracking for low tracking gains. (a) No friction ($\mu \times 0$). (b) Plant friction ($\mu \times 1$). (c) Plant friction overestimated ($\mu \times 2$).

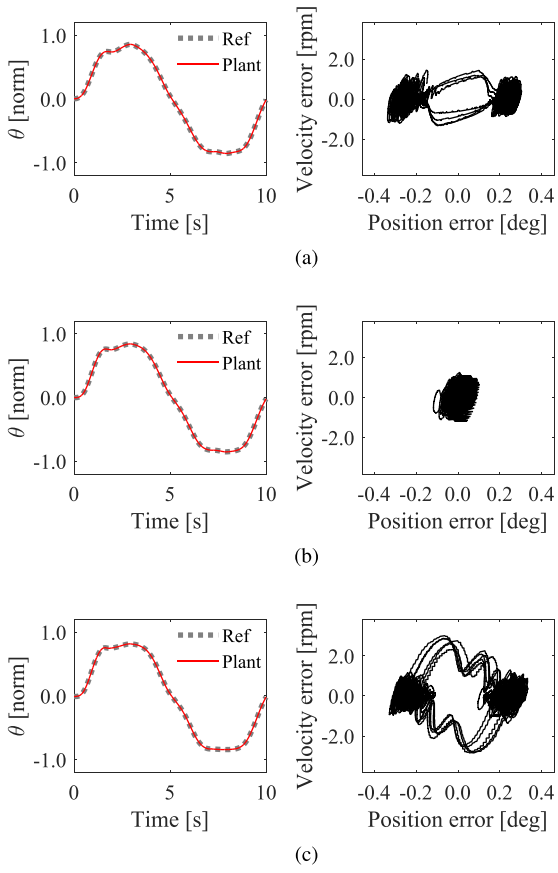

Fig. 15. Angular tracking for high tracking gains. (a) No friction ($\mu \times 0$). (b) Plant friction ($\mu \times 1$). (c) Plant friction overestimated ($\mu \times 2$).

as already analyzed in [35]. The responses to a sinusoidal torque input (amplitude 1.5 Nm and frequency 0.1 Hz) are shown for two sets of control gains.

1) Low Tracking Gains: The reference tracking gains are reduced by setting C_2 to 3 Hz (C_1 is kept at 110 Hz).

The column angular response is shown in Fig. 14 for the different values of the observer parameters. The plant and the reference responses are compared in the left plots, while the phase trajectories of the tracking error (position versus velocity) are represented in the right plots.

As expected, when the observer parameters are equal to the identified friction parameters (factor 1), the tracking error is minimum. When the friction is underestimated (factor 0) or overestimated (factor 2), the tracking error increases and a limit cycle is created in the phase plane (clockwise or counterclockwise, respectively). The two diametrically opposed accumulation points correspond to the sliding (or coulomb) regime for positive and negative velocities, where the undercompensation or overcompensation of friction results in a constant angular tracking error.

2) High Tracking Gains: C_2 is set back to 30 Hz.

The equivalent plots are shown in Fig. 15. It can be seen that the error is drastically reduced compared with that of Fig. 14. Again, the error is smaller when the observer parameters are equal to the identified plant parameters. In the three cases, the tracking error remains smaller than 0.5° in angular position and 3 r/min in angular velocity.

E. Controller's Contributions

The output (33) of the designed controller is composed of the term from the friction model in the internal loop plus the reference tracking term from the external loop. In Fig. 16, the contributions of each term for the case of high tracking gains (Fig. 15) are shown.

When the friction model is deactivated [Fig. 16(a)], the correction is entirely done by the reference model tracking controller. In particular, the tracking torque compensates the system friction and changes sign depending on the friction direction (sign of the velocity). When the friction model is active with the identified parameters [Fig. 16(b)], it contributes to most of the compensation of the plant friction and the reference tracking torque only corrects the errors due to friction irregularities. Finally, when the friction is twice overestimated [Fig. 16(c)], the reference tracking controller counteracts the overcompensation of friction with an opposite torque.

The experimental results shown in Figs. 14–16 confirm the conclusion of the robustness analysis in Section VI-C. The use of a reference model compensates for friction modeling error and ensures the controller robustness. In particular, even when the friction model loop is deactivated, a good tracking performance can still be ensured provided that the reference correction gains are high enough. However, having an accurate friction model in the internal loop reduces the tracking error.

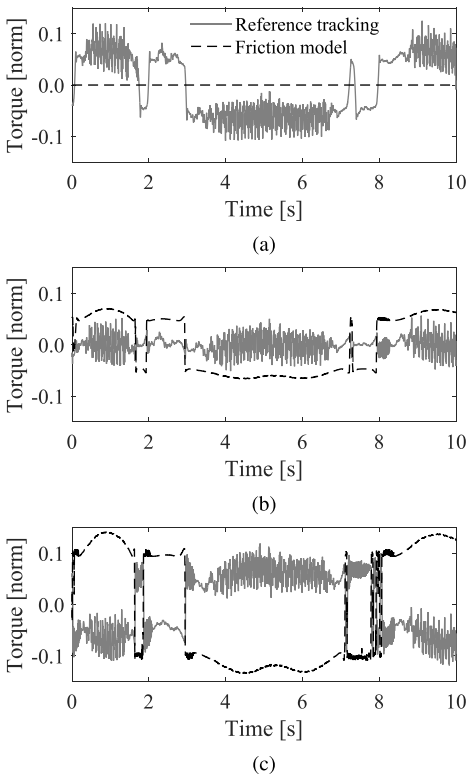

Fig. 16. Contribution of the two controllers to high tracking gains. (a) No friction ($\mu \times 0$). (b) Plant friction ($\mu \times 1$). (c) Plant friction overestimated ($\mu \times 2$).

VIII. Conclusion

In this paper, a control strategy for compensating friction in a C-EPS power column has been presented and validated experimentally. The control concept results from a long-term research project including power column modeling (simulation model), model validation against the experimental results, reduction of the complete model into a low-order model and finally the development and validation of the model-based control strategy. The modeling takes advantage of a slip- and load-dependent friction representation using the LuGre model.

The control strategy uses the assist motor of the EPS to compensate the estimated friction torque. It is composed of two cascaded loops. The internal loop contains a system observer based on the reduced model. This observer estimates the power column state, including the friction forces, using the two sensors of the power column (torsion bar and motor angular sensor). The estimated friction torque is then oppositely added to the motor torque command. The external loop realizes an angular control of the power column. The ideal angular response of the system without friction is computed from a reference model and a linear controller is applied to minimize the error between the plant and the reference responses. It is formally shown that the control strategy is able to track the plant trajectory with an error that can be controlled and made arbitrarily small with appropriate values of the gains.

The resulting control strategy is tested on a mass-produced power column using the actual sensors and signals. Compared with the open-loop response, the response of the power column mimics that of the ideal frictionless system. Due to the high values of the gains for the reference tracking loop, a very good tracking performance is achieved, including robustness against inaccurate friction parameters. This is made possible by the high quality of the sensors and actuator available in the system as well as the simplicity of the load used (spring damper). In practice, the load torque generated in an actual car is more complex and its estimation is a real challenge.

Using this control strategy to obtain a linear response of the power column, the development and tuning of higher level assistance strategies, including the appropriate amount of hysteresis necessary to ensure an optimal driving feel, are expected to be facilitated.

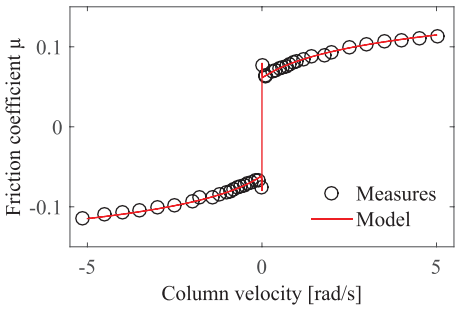

Fig. 17. Identification of the steady-state friction coefficient.

Appendix A
Friction Parameter Identification

The main unknown parameters of the system are those of the LuGre model (17). The parameters μ_{ba}, μ_c, and v_{stb} and the viscous friction $f(v_s)$ are static parameters, which affect the steady-state value of z for a given sliding velocity, while σ_0 and σ_1 are the parameters that affect the dynamics of z.

To identify the static parameters, the torque necessary to rotate the power column is measured at different steady-state velocity conditions, corresponding to different sliding velocities. This resisting torque is assumed to correspond to the friction of the LuGre model in steady state

$$\mu_{\text{ss}} = \mu_c + (\mu_{\text{ba}} - \mu_c)e^{-\left(\frac{v_s}{v_{\text{stb}}}\right)^2} + f(v_s). \tag{42}$$

The parameters μ_{ba}, μ_c, and v_{stb} are tuned for fitting the measures (Fig. 17). It can be seen that the identified viscosity $f(v_s)$ is nonlinear and is fitted with a logarithmic function, but can be approximated linearly for small velocities.

The identification of dynamic parameters (σ_0 and σ_1) is much more difficult, since they are hard to measure. The existing methods include frequency-domain identification [37] or genetic algorithms [38]. Here, the parameters have been manually tuned to obtain an appropriate response.

Appendix B
Contact State dh in Steadystate

In the gear-mesh model (Fig. 6), the contact condition is determined by dh, which represents the relative position of the engaged worm gear tooth within two worm wheel teeth. In the reduced model (Section IV), the contact dynamics of the gear mesh is neglected, which is equivalent to assuming that it is always in steady state. Therefore, the contact condition

dh should be computed in steady state, given the external load of the worm drive.

To this end, the external torque on the worm wheel is noted $T_{\mathrm{ww}} = T_{\mathrm{tb}} + T_{\mathrm{ls}}$. On the worm gear side, the inertia is $J_{\mathrm{wg}} + J_{\mathrm{ms}}$ (lumped worm gear and motor shaft inertia) and the external torque T_{ms} (motor shaft torque).

In steady state, the identity $\theta_{\mathrm{ww}} \equiv i\,\theta_{\mathrm{wg}} \equiv i\,\theta_{\mathrm{ms}}$ is verified. Using this identity with (2)–(4), it can be seen that

$$\begin{aligned}&\frac{1}{J_{\mathrm{ww}}}(T_{\mathrm{ww}} + r_{\mathrm{ww}} c\gamma\, c\beta F_C(dh) - r_{\mathrm{ww}}\mu s\gamma\, F_N(dh))\\ &= \frac{1}{i(J_{\mathrm{wg}} + J_{\mathrm{ms}})}(T_{\mathrm{ms}} - r_{\mathrm{wg}} s\gamma\, c\beta F_C(dh) - r_{\mathrm{wg}}\mu c\gamma\, F_N(dh))\end{aligned} \tag{43}$$

where $c\gamma = \cos(\gamma)$, $s\gamma = \sin(\gamma)$, and $c\beta = \cos(\beta)$.

Solving this equation is difficult due to the piecewise formulation of F_C and F_N. However, it can be simplified by assuming that the friction terms $\mu F_N(dh)$ are negligible compared with the contact force $F_C(dh)$. Under this assumption, (43) becomes

$$F_C(dh) = \frac{i\,J_{\mathrm{ww}} T_{\mathrm{ms}} - i^2(J_{\mathrm{wg}} + J_{\mathrm{ms}})(T_{\mathrm{ww}})}{r_{\mathrm{ww}}\cos(\gamma)\cos(\beta) J}. \tag{44}$$

The inverse function F_C^{-1} is then easy to compute [Fig. 7(a)].

Appendix C
Impulse Response of the Error System

The impulse response f of the critically damped second-order system

$$\ddot{x} + 2c\dot{x} + c^2 x = u \tag{45}$$

where $c > 0$, input u and output x are the inverse Laplace transform of the transfer function

$$f(t) = L^{-1}\left[\frac{1}{(s+c)^2}\right] = te^{-\frac{c}{2}t}.$$

Consider system (35) in the critically damped case (40)

$$\begin{aligned}\ddot{\varphi} + 2C_1\dot{\varphi} + C_1^2\varphi &= \frac{u(t)}{J}\\ \ddot{\tilde{\varphi}} + 2C_2\dot{\tilde{\varphi}} + C_2^2\tilde{\varphi} &= \frac{l_p}{J}\varphi + \frac{l_v}{J}\dot{\varphi}.\end{aligned} \tag{46}$$

The solutions of (46) with null initial conditions zero are

$$\varphi = h_1 * u, \quad \dot{\varphi} = \dot{h}_1 * u, \quad \tilde{\varphi} = h_2 * (l_p\varphi + l_v\dot{\varphi})$$

with

$$\begin{aligned}h_1(t) &= J^{-1}te^{-\frac{C_1}{2}t}\\ \dot{h}_1(t) &= J^{-1}(1 - C_1 t)e^{-\frac{C_1}{2}t}\\ h_2(t) &= J^{-1}te^{-\frac{C_2}{2}t}.\end{aligned}$$

The impulse response of (46) with input u and output $\theta - \hat{\theta} = \varphi + \tilde{\varphi}$ is thus given by

$$h = h_1 + h_2 * (l_p h_1 + l_v\dot{h}_1). \tag{47}$$

Recalling [36, p. 199] that $\|h_1 * h_2\|_{\mathcal{L}_1} \le \|h_1\|_{\mathcal{L}_1}\|h_2\|_{\mathcal{L}_1}$, the norm of h verifies

$$\|h\|_{\mathcal{L}_1} \le \|h_1\|_{\mathcal{L}_1} + \|h_2\|_{\mathcal{L}_1}(l_p\|h_1\|_{\mathcal{L}_1} + l_v\|\dot{h}_1\|_{\mathcal{L}_1}).$$

Using

$$\begin{aligned}\|h_1\|_{\mathcal{L}_1} &= J^{-1}C_1^{-2}\\ \|\dot{h}_1\|_{\mathcal{L}_1} &= J^{-1}2C_1^{-1}e^{-1}\\ \|h_2\|_{\mathcal{L}_1} &= J^{-1}C_2^{-2}\end{aligned}$$

and noting that $l_p \le JC_1^2$ and $l_v \le 2JC_1$, the bound

$$\|h\|_{\mathcal{L}_1} \le \frac{1}{JC_1^2} + \frac{1 + 4e^{-1}}{JC_2^2} \tag{48}$$

is obtained.

References

[1] C. Morton, C. M. Spargo, and V. Pickert, "Electrified hydraulic power steering system in hybrid electric heavy trucks," *IET Elect. Syst. Transp.*, vol. 4, no. 3, pp. 70–77, Sep. 2014.

[2] H. Miyazaki, "Technical trends in steering systems," in *Proc. 7th JFPS Int. Symp. Fluid Power*, Toyama, Japan, Sep. 2008, pp. 133–136.

[3] A. Badawy, J. Zuraski, F. Bolourchi, and A. Chandy, "Modeling and analysis of an electric power steering system," in *Proc. Steering Suspension Technol. Symp.*, 1999, paper 1999-01-0399.

[4] J. T. Illán, V. Ciarla, and C. C. de Wit, "Oscillation annealing and driver/tire load torque estimation in electric power steering systems," in *Proc. IEEE Int. Conf. Control Appl.*, Denver, CO, USA, Sep. 2011, pp. 1100–1105.

[5] A. T. Zaremba, M. K. Liubakka, and R. M. Stuntz, "Vibration control based on dynamic compensation in an electric power steering system," in *Proc. 1st Int. Conf. Control Oscillations Chaos*, vol. 3. St. Petersburg, Russia, Aug. 1997, pp. 453–456.

[6] R. C. Chabaan and L. Y. Wang, "Control of electrical power assist systems: H^∞ design, torque estimation and structural stability," *JSAE Rev.*, vol. 22, no. 4, pp. 435–444, Oct. 2001.

[7] N. Sugitani, Y. Fujuwara, K. Uchida, and M. Fujita, "Electric power steering with H-infinity control designed to obtain road information," in *Proc. Amer. Control Conf.*, vol. 5. Jun. 1997, pp. 2935–2939.

[8] T. Kifuku and S. Wada, "An electric power-steering system," *Mitsubishi Electr. Adv.*, vol. 78, pp. 20–23, Mar. 1997.

[9] T. Tamura, A. Maroonian, M. Higashi, and R. Fuchs, "Modeling and simulation for the dynamic analysis of an electric power steering," in *Proc. 3rd Int. Munich Chassis Symp.*, Munich, Germany, Jun. 2012.

[10] T. Tamura, A. Maroonian, and R. Fuchs, "Active compensation of friction in electric power steering," in *Proc. FISITA*, Beijing, China, Nov. 2012, pp. 213–225.

[11] A. Marouf, M. Djemai, C. Sentouh, and P. Pudlo, "A new control strategy of an electric-power-assisted steering system," *IEEE Trans. Veh. Technol.*, vol. 61, no. 8, pp. 3574–3589, Oct. 2012.

[12] Z. He and M. Gu, "Dynamic research on control strategy of electric power steering system," in *Proc. SAE World Congr.*, 2012, doi: 10.4271/2012-01-0212.

[13] M. Heger and A. Heilig, "Verfahren zum Betrieb eines Lenksystems in einem Kraftfahrzeug," German Patent DE102 007 006 232 A1, Aug. 14, 2008.

[14] S. Endo, "Control unit for electric power steering apparatus," U.S. Patent 6 744 232 B2, Jun. 1, 2004.

[15] H. Olsson, K. J. Åström, C. C. de Wit, M. Gäfvert, and P. Lischinsky, "Friction models and friction compensation," *Eur. J. Control*, vol. 4, no. 3, pp. 176–195, 1998.

[16] M. Salaani, G. Heydinger, and P. Grygier, "Experimental steering feel performance measures," in *Proc. SAE World Congr.*, 2004, doi: 10.4271/2004-01-1074.

[17] J. Zhao *et al.*, "Optimal design of off-center steering characteristics based on subjective evaluation," in *Proc. FISITA*, Maastricht, The Netherlands, Jun. 2014.

[18] I. Kushiro, S. Koumura, and H. Kawai, "A new approach in the study on-center handling," in *Proc. 9th Int. Symp. Adv. Veh. Control*, Kobe, Japan, Oct. 2008.

[19] Y.-H. J. Hsu, S. M. Laws, and J. C. Gerdes, "Estimation of tire slip angle and friction limits using steering torque," *IEEE Trans. Control Syst. Technol.*, vol. 18, no. 4, pp. 896–907, Jul. 2010.

[20] H. Chen, L. Zhang, and B. Gao, "Active return control of EPS based on model reference fuzzy adaptive control," in *Proc. IEEE Int. Conf. Mechatronics*, Istanbul, Turkey, Apr. 2011, pp. 194–199.

[21] A. Zaremba and R. I. Davis, "Dynamic analysis and stability of a power assist steering system," in *Proc. Amer. Control Conf.*, vol. 6. Seattle, WA, USA, Jun. 1995, pp. 4253–4257.

[22] P. E. Pfeffer, M. Harrer, and D. N. Johnston, "Modelling of a hydraulic steering system," in *Proc. FISITA*, Yokohama, Japan, 2006.

[23] R. Pastorino, M. A. Naya, J. A. Pérez, and J. Cuadrado, "X-by-wire vehicle prototype: A steer-by-wire system with geared PM coreless motors," in *Proc. 7th EUROMECH Solid Mech. Conf.*, Lisbon, Portugal, Sep. 2009, pp. 1–3.

[24] M. E. Dohring, E. Lee, and W. S. Newman, "A load-dependent transmission friction model: Theory and experiments," in *Proc. IEEE Int. Conf. Robot. Autom.*, vol. 3. Atlanta, GA, USA, May 1993, pp. 430–436.

[25] C. C. de Wit, H. Olsson, K. J. Åström, and P. Lischinsky, "A new model for control of systems with friction," *IEEE Trans. Autom. Control*, vol. 40, no. 3, pp. 419–425, Mar. 1995.

[26] H. Olsson, "Control systems with friction," Ph.D. dissertation, Dept. Automat. Control, Lund Univ., Lund, Sweden, 1996.

[27] M. Aberger and M. Otter, "Modeling friction in modelica with the Lund-Grenoble friction model," in *Proc. 2nd Int. Modelica Conf.*, Oberpfaffenhofen, Germany, Mar. 2002, pp. 285–294.

[28] L. Lu, B. Yao, Q. Wang, and Z. Chen, "Adaptive robust control of linear motor systems with dynamic friction compensation using modified LuGre model," in *Proc. IEEE/ASME Int. Conf. Adv. Intell. Mechatronics*, Xi'an, China, Jul. 2008, pp. 961–966.

[29] G. Rill, *Road Vehicle Dynamics: Fundamentals and Modeling* (Ground Vehicle Engineering Series). New York, NY, USA: Taylor & Francis, Sep. 2011.

[30] F. Nenglian, P. Jiankun, Z. Xiaolong, Y. Jiawang, and T. Yanrong, "Research on electric power steering system simulation based on 3-DOF vehicle model," in *Proc. Int. Conf. Transp. Mech. Elect. Eng.*, Changchun, China, Dec. 2011, pp. 821–824.

[31] T. Yang, "A new control framework of electric power steering system based on admittance control," *IEEE Trans. Control Syst. Technol.*, vol. 23, no. 2, pp. 762–769, Mar. 2015.

[32] J.-H. Kim and J.-B. Song, "Control logic for an electric power steering system using assist motor," *Mechatronics*, vol. 12, no. 3, pp. 447–459, Apr. 2002.

[33] S. Amberkar, F. Bolourchi, J. Demerly, and S. Millsap, "A control system methodology for steer by wire systems," in *Proc. SAE World Congr.*, 2004.

[34] D. Putra and H. Nijmeijer, "Limit cycling in observer-based controlled mechanical systems with friction," in *Proc. Eur. Control Conf.*, Cambridge, U.K., Sep. 2003, pp. 312–317.

[35] D. Putra, H. Nijmeijer, and N. van de Wouw, "Analysis of undercompensation and overcompensation of friction in 1DOF mechanical systems," *Automatica*, vol. 43, no. 8, pp. 1387–1394, 2007.

[36] H. K. Khalil, *Nonlinear Systems*, 3rd ed. Englewood Cliffs, NJ, USA: Prentice-Hall, 2002.

[37] R. H. A. Hensen, M. J. G. van de Molengraft, and M. Steinbuch, "Frequency domain identification of dynamic friction model parameters," *IEEE Trans. Control Syst. Technol.*, vol. 10, no. 2, pp. 191–196, Mar. 2002.

[38] D.-P. Liu, "Parameter Identification for LuGre friction model using genetic algorithms," in *Proc. Int. Conf. Mach. Learn. Cybern.*, Dalian, China, Aug. 2006, pp. 3419–3422.

Frédéric Wilhelm received the Diplôme d'Ingénieur from École Polytechnique, Palaiseau, France, in 2011, and the M.S. degree in microengineering from the École Polytechnique Fédérale de Lausanne, Lausanne, Switzerland, in 2013.

He has been with the Advanced Creative Technology Research Department, JTEKT Corporation, Nara, Japan, since 2014. His current research interests include modeling and control of steering systems, vehicle dynamics, advanced driving assistance systems, and autonomous driving.

Mr. Wilhelm has first developed this friction compensation algorithm during his master's project in 2013 and received the Best Master Thesis Award from the Swiss Society for Automatic Control.

Tsutomu Tamura received the B.S. and M.S. degrees from the University of Shiga Prefecture, Hikone, Japan, in 2001 and 2004, respectively.

He has been with JTEKT Corporation, Nara, Japan, since 2004, where he has been an Assistant Manager with the Advanced Creative Technology Research Department since 2011. His current research interests include modeling and control of driveline components and steering systems, vehicle dynamics, advanced driving assistance systems, and autonomous driving technologies.

Robert Fuchs (M'06) received the B.S. degree from the École d'Ingénieurs de Genève, Geneva, Switzerland, in 1993, and the M.S. degree from the École Polytechnique Fédérale de Lausanne (EPFL), Lausanne, Switzerland, in 1997.

He joined JTEKT Corporation, Nara, Japan, in 2000. He conducted his Ph.D. research on the control of a continuous variable transmission in collaboration with EPFL from 2002 to 2006. He has led several research projects about modeling and control of driveline components and steering systems. Since 2012, he has been the Director of Technology and Innovation with the Research and Development Center, JTEKT Corporation, Paris, France, where he is leading the EU Representative Office.

Philippe Müllhaupt (M'04) received the Diplôme d'Ingénieur in electrical engineering from the École Polytechnique Fédérale de Lausanne (EPFL), Lausanne, Switzerland, in 1993, the Diplôme d'études Approfondies in signal processing and control theory from the University of Paris XI, Orsay, France, in 1994, and the Ph.D. degree in nonlinear control with an application to underactuated mechanical systems from EPFL, in 1999.

He joined the European Nonlinear Control Network, Centre Automatique et Systèmes, École Nationale Supérieure des Mines de Paris, Fontainebleau, France, as a Post-Doctoral Fellow. He is currently with the Institute of Mechanical Engineering, EPFL, where he collaborates with the Laboratoire d'Automatique, the Swiss Space Center, and the Biorobotics Laboratory. He is also a Lecturer for classical mechanics, nonlinear control, linear control, and multivariable state space methods. His current research interests include geometric and algebraic methods for nonlinear control systems.